Sodiation *via* Heterogeneous Disproportionation in FeF_2 Electrodes for Sodium-Ion Batteries

Kai He,[†] Yongning Zhou,[‡] Peng Gao,[§] Liping Wang,[§] Nathalie Pereira,[‖] Glenn G. Amatucci,[‖] Kyung-Wan Nam,[⊥] Xiao-Qing Yang,[‡] Yimei Zhu,[#] Feng Wang,[§,*] and Dong Su[†,*]

[†]Center for Functional Nanomaterials, Brookhaven National Laboratory, Upton, New York 11973, United States, [‡]Chemistry Department, Brookhaven National Laboratory, Upton, New York 11973, United States, [§]Sustainable Energy Technologies Department, Brookhaven National Laboratory, Upton, New York 11973, United States, [‖]Department of Materials Science and Engineering, Rutgers University, North Brunswick, New Jersey 08902, United States, [⊥]Department of Energy and Materials Engineering, Dongguk University-Seoul, Seoul 100-715, Republic of Korea, and [#]Department of Condensed Matter Physics and Materials Science, Brookhaven National Laboratory, Upton, New York 11973, United States

ABSTRACT **Sodium-ion batteries utilize various electrode materials derived from lithium batteries. However, the different characteristics inherent in sodium may cause unexpected cell reactions and battery performance. Thus, identifying the reactive discrepancy between sodiation and lithiation is essential for fundamental understanding and practical engineering of battery materials. Here we reveal a heterogeneous sodiation mechanism of iron fluoride (FeF_2) nanoparticle electrodes by combining *in situ/ex situ* microscopy and spectroscopy techniques. In contrast to direct one-step conversion reaction with lithium, the sodiation of FeF_2 proceeds *via* a regular conversion on the surface and a disproportionation reaction in the core, generating a composite structure of 1–4 nm ultrafine Fe nanocrystallites (further fused into conductive frameworks) mixed with an unexpected Na_3FeF_6 phase and a NaF phase in the shell. These findings demonstrate a core–shell reaction mode of the sodiation process and shed light on the mechanistic understanding extended to generic electrode materials for both Li- and Na-ion batteries.**

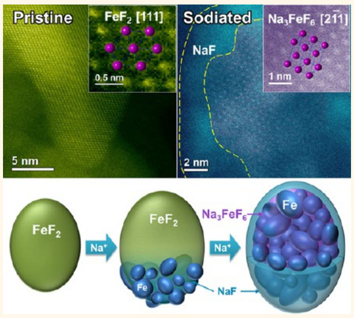

KEYWORDS: sodium-ion battery · *in situ* TEM · disproportionation · sodiation · FeF_2 · Na_3FeF_6 · heterogeneous reaction

Advances in portable electronic devices have stimulated the growing market of rechargeable batteries, in particular Li-ion batteries (LIBs).[1] For emerging large-scale applications, such as electric vehicles and power grid storage,[2,3] the issues of limited natural abundance of lithium resource and thus price increases will inevitably arise in the near future.[4] With such increasing demand of energy storage, alternative technologies have been widely explored, one of which focuses on Na-ion batteries (NIBs) due to the large abundance and low cost of sodium.[5−7] As a neighboring alkali metal in the periodic table, sodium shares great similarity with its lithium analogue, implying that the insights obtained from the LIB studies may be presumably applicable to the development of NIBs. Nevertheless, it is also necessary to take the fact into account that the sodium ion has a fairly larger radius and heavier mass, which would directly affect the ion transport and the correlated electrochemical process with respect to the positive/negative electrodes. For example, the electrode materials with layered or tunneled structures used in the current LIB technology (*e.g.*, graphite) may not have enough space to accommodate the reversible intercalation of Na^+ ions and, thus, are unable to function well in the NIB system.[8] However, in contrast to the intercalation materials, another type of mechanism based on conversion reactions between alkali metals and electrode materials does not primarily rely on the size of alkali cations and can also accommodate multiple-electron transfer per formula unit, offering a promising strategy toward high-capacity electrodes for NIBs.[9,10]

Conversion reactions have been studied a long time ago for primary batteries and were revived after the demonstration of reversible electrochemical reactivity in rechargeable LIB cells by Tarascon and co-workers.[11] Since then, they started attracting more

* Address correspondence to
D. Su
(dsu@bnl.gov) or
F. Wang
(fwang@bnl.gov).

Received for review April 26, 2014
and accepted June 9, 2014.

10.1021/nn502284y

attention in searching for appropriate conversion compounds in the form of binary transition metal (M = Fe, Co, Ni, Cu, Mn, *etc.*) oxides, sulfides, nitrides, phosphides, and fluorides.[9] The majority of efforts have been focused on conversion reactions with lithium, whereas only a few compounds were experimentally examined for sodium-ion technology, such as FeS_2, Cu_2S, Ni_3N, and FeF_3.[12−15] Most conversion compounds were used as anodes because of their relatively low operating potentials *vs* Li/Li^+ (or Na/Na^+), except for fluorides such as iron fluorides (FeF_2 and FeF_3), which have been found to exhibit higher output potentials and therefore are suitable for use as cathodes.[16−20] In a recent work on the conversion reaction of FeF_2 with Li, the high reversibility in FeF_2 was attributed to formation of a percolating iron network for electron transport.[19] Whether or not FeF_2 can be functionally adapted to the sodium-ion technology and what reaction mechanism lies therein remain open questions and motivate the present study.

In situ transmission electron microscopy (TEM) has been recognized as a powerful tool to perform real-time observation of electrochemical reactions of electrode materials with lithium and sodium on the nanometer scale.[20−25] The *in situ* cell first built by Huang *et al.* is mostly used for investigating individual nanostructured electrodes, and the targeting materials typically require special geometry, *i.e.*, nanowires.[22] For examining electrochemical processes and associated structural evolution more realistically in general composite electrodes, Wang *et al.* further developed another format that uses a composite mixing the targeting materials with the carbon, as both support and media for ion and electron transport.[20] Despite these technical details, the effort so far spent on *in situ* sodium battery research is substantially less than that on its lithium counterpart,[24−26] encouraging us to add lacking knowledge in particular to the sodium conversion system to address the differential reaction mechanism and kinetics stemming from the inherent characteristics of sodium. In this study, we utilized the latter of the aforementioned configurations to study the phase transition and electrochemical reaction during sodiation as well as the morphology evolution of individual FeF_2 nanoparticles (NPs) using advanced analytical electron microscopy techniques. Our results for the first time provided the direct experimental evidence of a new reaction pathway during lithium/sodium ion insertion, which was previously predicted from theoretical calculation.

RESULTS AND DISCUSSION

The reversible electrochemical reactivity of FeF_2 with sodium has been verified by coin-cell battery tests (Figure 1g), which show a specific capacity of ∼190 mAh/g for the first discharge, about one-third of its theoretical capacity (571 mAh/g) as based on two-electron transfer per FeF_2.[19] This subpar performance may be attributed to a special reaction mechanism dissimilar to the regular conversion reaction in LIB. To uncover the origin of such different behavior, we carried out an *in situ* TEM study. FeF_2 NPs dispersed on amorphous carbon support were incorporated into an *in situ* TEM cell and reacted with a sodium counter electrode (Figure 1a, details described in the Methods session). The real-time morphology evolution of FeF_2 NPs upon sodiation was captured with subsecond temporal resolution using high-angle annular dark-field (HAADF) imaging in STEM mode, as shown in Figure 1 and Movie S1 (see Supporting Information). Figure 1b and c show the HAADF-STEM images of pristine and fully sodiated FeF_2 NPs, respectively. The pristine particles are ellipsoids with an average size around 10−20 nm, while the sodiated particles display great morphological distinction with numerous ∼2 nm nanocrystallites (Fe, as evidenced in a later discussion) uniformly dispersed in the expanded particle matrix. We selected four individual particles (labeled 1−4) and one aggregated cluster (labeled 5) from the field of view, and by comparing their size changes before and after the sodiation we found that all the FeF_2 NPs exhibit a similar radial expansion of ∼30% regardless of the initial sizes, as shown in Figure 1e. It is worth noting that this value is dramatically less than the expansion of Sn NPs upon sodiation through the alloying mechanism[24] and on the similar order of magnitude to that of lithiated FeF_2 NPs *via* conversion reaction.[20] We further focus on the particles 1−3, whose geometrical boundaries are trackable with clear STEM contrast, to reveal the propagation of the reaction front and kinetics during sodiation, as in the time-lapse snapshots displayed in Figure 1d. The reaction processes of particles 1 and 2 are similarly straightforward, during which the reaction front traverses from one end (on the carbon support) to the other (suspended in vacuum) as a result of Na migration along the same pathway, as indicated by the yellow arrows. The reaction in particle 3 proceeds more sophisticatedly: the reaction fronts simultaneously propagate from the immediately connected just-sodiated NPs until they merge upon completion of sodiation. These two phenomenal scenarios together describe a 2-fold mechanism, that is, volume-diffusion-controlled sodium transport within a single separate NP and interface-involved interparticle transport for closely packed NP networks, which would both be expected to occur in real electrodes. The effective interparticle Na transport mechanism allows sodiation to proceed thoroughly even to the material untouched by electrolyte in a real cell. Furthermore, we conducted quantitative analysis on the three particles by clipping the frames right from the exact reaction beginning on its own. The two-dimensional (2D) areal sizes were measured as a function of the actual reaction time, and

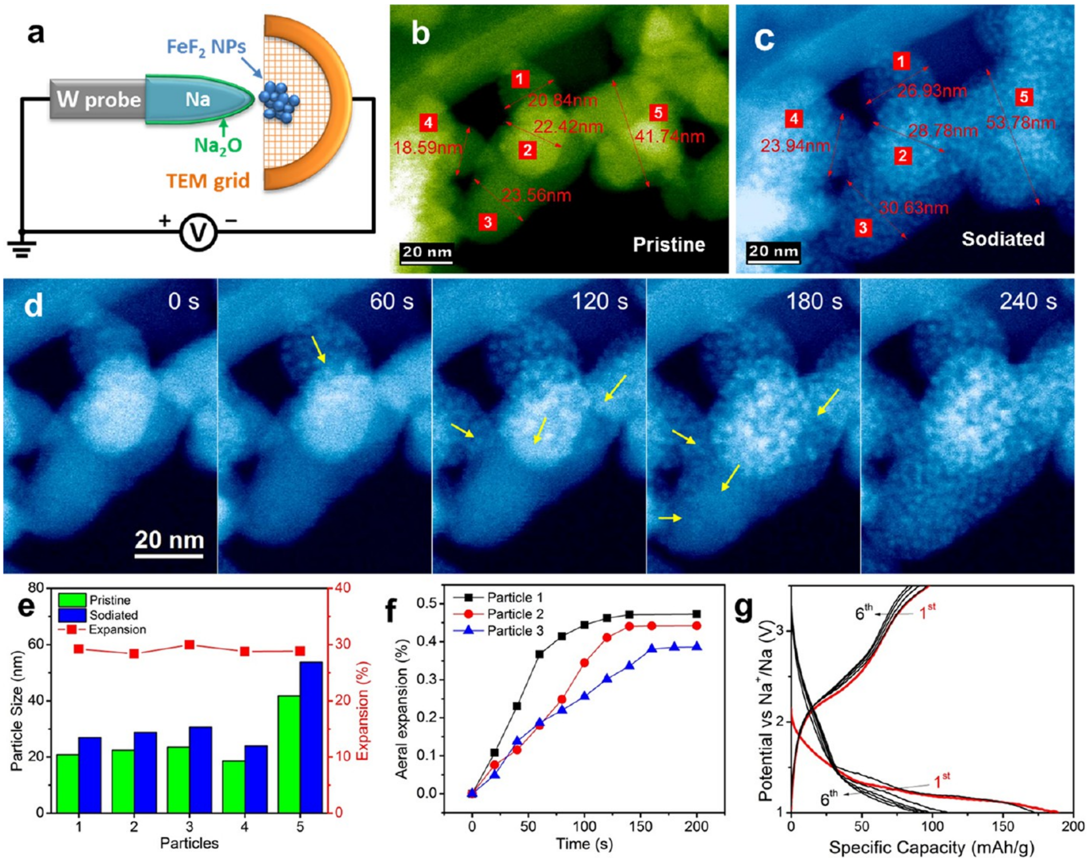

Figure 1. (a) Schematic showing the setup of the *in situ* experiment. HAADF-STEM images showing (b) pristine and (c) sodiated FeF$_2$ NPs and (d) cropped time-lapse frames throughout the sodiation process. (e) Plot showing particle sizes and radial expansions before and after sodiation. (f) Plot of normalized areal size expansion as a function of respective reaction time for particles 1–3. (g) Charge–discharge profiles of a FeF$_2$/Na coin cell during the first 6 cycles (1st cycle in red). The red labels and double arrows in panels (b) and (c) correspond to the analysis in (e). The yellow arrows in panel (d) indicate the directions of the sodiation propagation that starts from one end of the particles on the carbon support.

the normalized areal expansions for the three particles are accordingly plotted in Figure 1f. It is noted that the size of each NP increases rapidly at the early nucleation stage and then gradually saturates at a plateau and that it takes more time to complete the reaction for a larger particle. Our findings suggest that the sodiation process is primarily dominated by the intrinsic volume diffusion of Na within the bulk of FeF$_2$ NPs.

We now turn our attention to the subsequent growth kinetics of the Fe nanocrystallites within one single FeF$_2$ NP. Figure 2a shows time-lapse HAADF-STEM images of a representative FeF$_2$ NP (as indicated by the dashed line) overlaying a carbon support during the first sodiation cycle (Movie S2, Supporting Information). It is observed that the Fe nanocrystallites precipitate and gradually populate the entire particle as the reaction front moves from the top-left to the bottom-right corner. We chose five representative image frames with a time duration of 0–240 s and interval of 60 s and measured the total number and each nanocrystallite's size for all these frames. The resulting histogram is plotted in Figure 2b with each set of nanocrystallite sizes statistically fit with a Gaussian distribution, revealing an increasing shift of the average size from 1.9 ± 0.3 nm to 2.5 ± 0.4 nm as well as an increase of quantity as a function of time. This time dependence of the growth is quantitatively described in Figure 2c. The quantity of Fe nanocrystallites exhibits a linear dependence on time, and the intersection with the time axis (−56 s) indicates that the actual sodiation beginning is rather prior to the starting point of the captured image series, consistent with the existence of a few nanocrystallites in the first frame. Interestingly, the plot of crystallite size *vs* reaction time can be fitted to a temporal power-law dependence, namely, t^n with $n = 0.15$, which follows the classic volume-diffusion-controlled coarsening behavior with a particular influence of precipitate–matrix interface kinetics.[27] As an approximation to the real NIB, the rapid sodiation (∼5 min, the same time scale as in lithiation) of individual FeF$_2$ NPs, equivalent to a local discharge rate of 12 C, enables the feasibility to achieve fast cycling, if proper engineering is used to expedite Na circulation between electrodes and active materials. Comparing to the lithiation of FeF$_2$ NPs,[20] the morphological evolution during sodiation is very similar, resulting in similar size distribution of formed Fe nanocrystallites, and both cases are governed by similar power laws, as compared in Figure 2d.

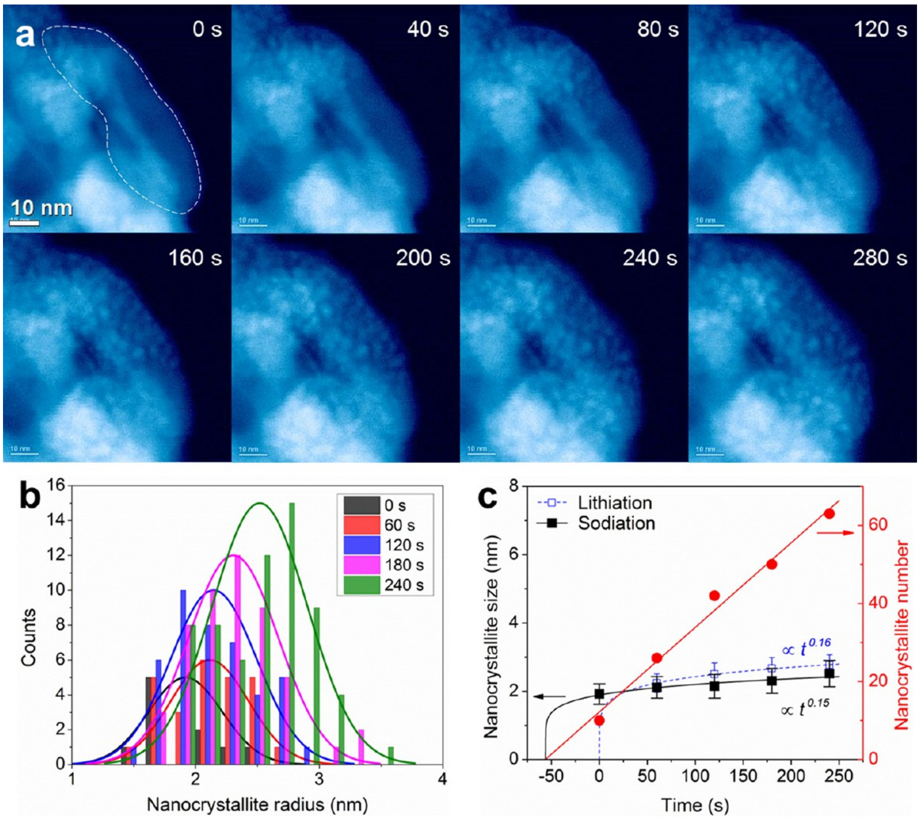

Figure 2. Growth kinetics of converted Fe nanocrystallites. (a) Time-lapse HAADF-STEM images showing the formation of Fe nanocrystallites within a single FeF_2 NP (indicated by a dashed line) upon sodiation. Scale bar, 10 nm. (b) Histogram showing statistical distribution of Fe nanocrystallites at recording times of 0, 60, 120, 180, and 240 s, respectively. The distribution curves are fit by a Gaussian function. (c) Plot of size (black squares) and number (red disks) of Fe nanocrystallites as a function of time. The number follows a linear dependence on time, and the size on a power law, t^n with $n = 0.15$. The size−time dependence for lithiation of FeF_2 NPs (open blue squares, data from ref 20) follows a similar power law, t^n with $n = 0.16$.

The global phase change upon sodiation and desodiation was examined by synchrotron X-ray diffraction (XRD, Figure S6 in the Supporting Information). However, no clear peaks other than those of FeF_2 from (de)sodiation products could be retrieved because the other sodiated phases are in the form of extremely small crystals or are amorphous. Nevertheless, benefiting from the stronger interaction between the electron and materials than that of X-rays, we were able to identify the evolution of the phase transition throughout the sodiation process using *in situ* electron diffraction (ED, Movie S3 in the Supporting Information). Figure 3a and b show TEM bright-field images of a collection of FeF_2 NPs from the same area before and after sodiation, respectively. The enlarged views of exact objects in the dashed-box regions depict the similar morphological change to that in HAADF images (Figures 1 and 2). ED patterns were recorded also from the same collection of particles in the pristine and sodiated states, as displayed in Figure 3c and d, respectively. The change from discrete diffraction rings to broadened and continuous Bragg rings indicates the transformation of pristine FeF_2 NPs into a large amount of ultrafine Fe nanocrystallites and Na-containing phase(s). By careful comparison of diffraction profiles in Figure 3d to a full survey of all possible Na-containing compounds (NaF, $NaFeF_3$, $NaFeF_4$, Na_2FeF_7, Na_3FeF_6, and $Na_5Fe_3F_{14}$), the sodiated phase(s) could be indexed to NaF or Na_3FeF_6,[28] or their mixture. Although an accurate identification of the sodium hexafluoroferrate (Na_3FeF_6) phase may not be conclusive solely from ED, the further analytical and high-resolution imaging evidence (discussed later) would support the existence of the two-phase mixture. A series of ED patterns were sequentially captured during the sodiating process, and the radial intensity profiles that were rotationally averaged over the entire 2π regime are listed in Figure 3e. Comparing the ED intensity changes upon sodiation, it is noticeably found that the FeF_2 peaks gradually diminish along with simultaneous emergence and subsequent increase of the Fe phase and NaF/Na_3FeF_6 mixture phase. From the normalized ED intensities, the relative quantities of these phases can be extracted as a function of time, as shown in Figure 3f. The quantitative tendency of phase evolution reveals that the majority of sodiation (>95%) was completed within 4 min in the observation area of 370 × 370 nm^2.

The insertion of Na ions can be tracked by electron energy-loss spectroscopy (EELS), from both the Na L-edge (at 31 eV) and the Fe M-edge (at 54 eV), as

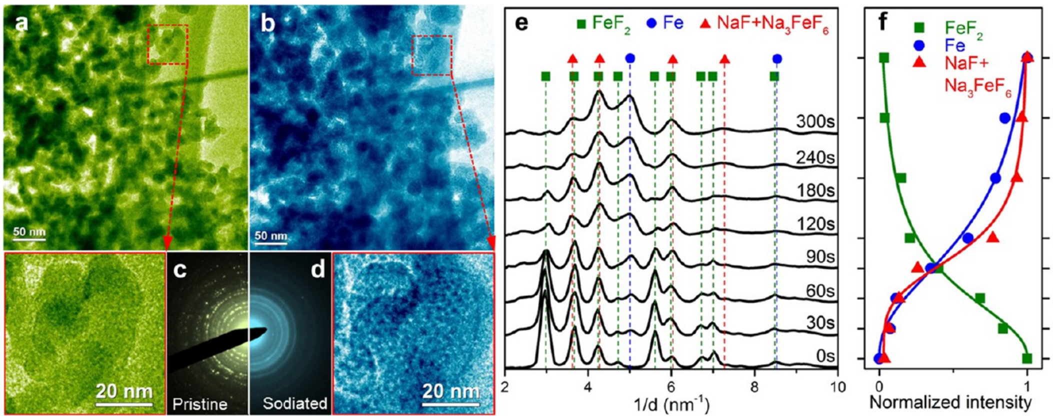

Figure 3. TEM bright-field images showing a number of FeF_2 NPs from the same area in (a) pristine and (b) sodiated states. The same particles in the dashed-box regions are enlarged at the lower-left and right corners. ED patterns recorded from (c) pristine and (d) sodiated particles. (e) Rotationally averaged intensity profiles obtained from time-sequenced ED patterns showing phase evolution upon sodiation. The ED peaks are indexed to phases of FeF_2 (squares), Fe (circles), and a mixture of NaF + Na_3FeF_6 (triangles). (f) Normalized quantitative phase evolution as a function of time, extracted from (e).

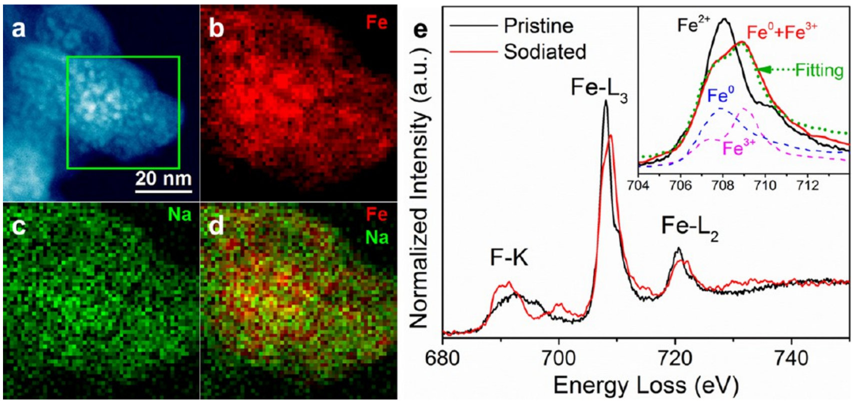

Figure 4. (a) STEM image of a sodiated NP. STEM-EELS elemental mapping (54 by 54 pixels, step ~7.1 Å) of (b) Fe and (c) Na elements from the boxed area in (a). (d) Composite elemental mapping showing the distribution of both Fe and Na. (e) EELS spectra of pristine and sodiated FeF_2 NPs, with inset showing the enlargement of the Fe L_3-edge. The sodiated Fe L_3-edge can be decomposed into two spectra corresponding to standard Fe^0 (blue dashed line) and Fe^{3+} (purple dashed line). The ratio of Fe^0/Fe^{3+} is ~70%:30%, determined by fitting the normalized standard spectra, as shown as a green dotted line.

shown in Figure S3 (see the Supporting Information). Using the STEM-EELS method,[29] we have examined the elemental distribution of the sodiated NPs. As seen in Figure 4a–d, the elemental distribution of Na (green) is uniformly across the sodiated NPs, whereas the Fe (red) element also suffuses the whole particle but is particularly enriched at the nanocrystallite spots. The combination of ED and EELS results attribute the newly formed nanocrystallites to Fe. The slightly larger distribution of Na than Fe suggests that a thin layer of NaF is on the surface of the inner Na_3FeF_6 phase (mixed with Fe nanocrystallites). EELS spectra of pristine and sodiated samples are compared in Figure 4e. F K-edge and Fe L-edges are clearly present in both samples, but there is some subtle change in the F K-edge that indicates the different states of bonding with Fe before and after sodiation. To identify the valence change in Fe upon sodiation, we investigated the near-edge fine structure of the Fe L_3-edge, as depicted in the inset of Figure 4e. Before sodiation, the Fe L_3-edge in pristine FeF_2 has a major peak at 708 eV and a minor bump at 710 eV, corresponding to a typical Fe^{2+} valence state.[30] In contrast, the sodiated sample shows a broad dichotomic L_3 peak shifted by about 1 eV toward higher energy, which can be decomposed into two peaks (shown as blue and purple dashed lines), corresponding to the standard Fe^0 and Fe^{3+} valence states, respectively.[30,31] The EELS evidence confirms the transformation from pristine Fe^{2+} to Fe^0 and Fe^{3+}, as well as the coexistence of Na_3FeF_6 and NaF phases after sodiation.

High-resolution STEM imaging was employed to observe the lattice structures of the involved species on the atomic scale, as shown in Figure 5a–c (also in Figure S3, Supporting Information). The atomic structures are clearly resolved in the real space and readily indexed to the standard model structures (Table S1, Supporting Information). While we confirmed that the pristine FeF_2 NPs are pure single-phase rutile crystals,

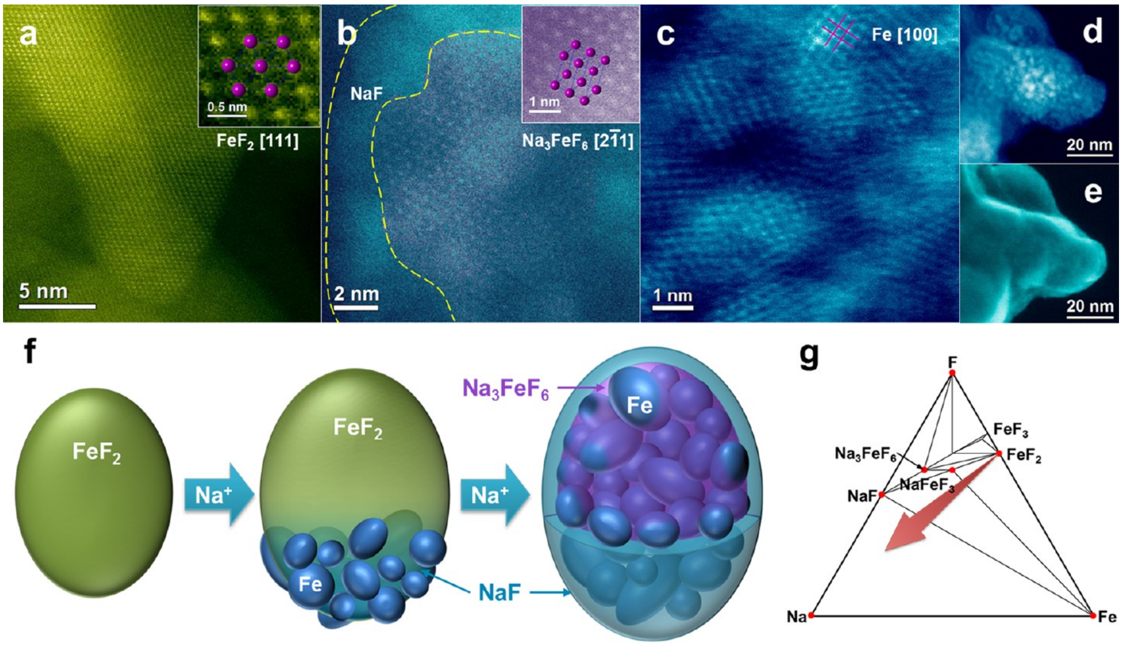

Figure 5. High-resolution STEM images showing (a) pristine FeF_2 NPs, (b) crystalline Na_3FeF_6 phase in the core of the sodiated particle, and (c) interconnected Fe nanocrystallites in the sodiated particle. The insets of (a) and (b) show close-up views matching with lattice models of FeF_2 (111) and Na_3FeF_6 (2−11). (d) HAADF-STEM and (e) STEM-SEM images of a same sodiated NP. (f) Schematic illustration of sodiation by a heterogeneous reaction mechanism. (g) Na−Fe−F phase diagram generated by DFT calculations at 0 K.[33]

we also found that the sodiated NPs are composed of Fe nanocrystallites embedded in the Na_3FeF_6 phase. The gentle granular contrast shown in the NaF layer is caused by the overlap of Fe nanocrystallites that are slightly out of focus. In addition, the Na_3FeF_6 phase is present only inside the core of the NP, consistent with our ED and EELS results. The metallic Fe nanocrystallites are interconnected as a conductive network, similar to the case in the Fe/LiF system, offering an effective pathway for electron transport.[19,20] Due to the transmission nature of the S/TEM technique, the acquired micrographs can only carry 2D intensity information integrated along the beam projection and are incapable of revealing how the converted Fe nanocrystallites distribute on the particle surface. As a complementary method, a unique high-resolution SEM imaging technique was used to acquire tomographic features of the particle surface.[32] In contrast to distinguishable Fe particles (within sodiated FeF_2 particles) in the projected HAADF images (Figure 5d), it is surprising to see the smooth surface of the same sodiated particles (Figure 5e). This suggests that the disproportionation sodiation proceeds mainly through the bulk (or volume), so that all the Fe nanocrystallites mixed in the Na_3FeF_6 matrix are covered by a layer of NaF from the surface conversion.

On the basis of the results from ED, EELS, and HR-STEM imaging, we suggest that the sodiation includes a regular conversion reaction on the NP surfaces (eq 1) and a novel disproportionation process (eq 2) inside the NP core, expressed as follows:

$$FeF_2 + 2Na^+ + 2e^- \rightarrow 2NaF + Fe \qquad (1)$$

$$FeF_2 + Na^+ + e^- \rightarrow \frac{1}{3}Na_3FeF_6 + \frac{2}{3}Fe \qquad (2)$$

In addition, from the EELS result of Figure 4e, the Fe^0/Fe^{3+} ratio can be estimated at 0.7:0.3 from that particular area, meaning that about 10% FeF_2 was converted into NaF and Fe, and the remaining 90% was disproportionated to Na_3FeF_6 and Fe, which is quantitatively rational for the core−shell reaction model. All of our *in situ* and *ex situ* results can be interpreted with a heterogeneous reaction mechanism for the sodiation process, as illustrated in Figure 5f. When sodium diffuses onto the FeF_2 NP, an excess of Na^+ ions is supplied to the local electrochemical environment favorable for simultaneous conversion between Na and FeF_2 to form ultrafine Fe nanocrystallites and a NaF layer on the surface of the FeF_2 particles. With further Na^+ diffusion, the reaction front propagates forward (lateral traverse) and inward (shell-to-core). In the latter case, due to fast surface diffusion, the surface reaction would likely be direct conversion, eventually leading to a complete NaF passivation shell on the particle surface, which hinders inward diffusion through the bulk, and thus the insufficient Na^+ supply would favor the disproportionation reaction to generate a crystalline Na_3FeF_6 phase in the core of the particle. In the meanwhile, as more Fe nanocrystallites precipitate, the bulk of the particle becomes less dense (*i.e.*, FeF_2 4.26 g/cm^3 to NaF 2.79 g/cm^3 and Na_3FeF_6 3.15 g/cm^3, JCPDS #45-1062, #36-1455, and #22-1381). As a result, the sodiated particle expands its volume to encapsulate the Fe nanocrystallites inside. This kind of composite can host more buffer space to retain mechanical integrity for reversible sodiation and desodiation, but the surface NaF layer may passivate the ionic diffusivity toward the unreacted particle core, which causes a low capacity as measured in coin cells. In our model, the overall heterogeneous reaction mechanism would result from the competition of diffusion pathways (surface *vs* bulk).

Although the *in situ* TEM cell can be used to visualize the reaction of the electrode materials under a certain electrochemical environment, we note that the electrochemical environment is not identical to the real battery cell. Therefore, correlation of *in situ* results to *ex situ* behavior of the same electrode material from a realistic battery is essential. In Figure S4 (see Supporting Information), we compared the morphology, phase, and chemical bondings between the *in situ* and coin-cell electrodes at the fully discharged (sodiated) state, and all these characteristics exhibit highly similar consistency. Moreover, quantitative EELS analysis indicates the Fe existing as ~90% Fe^0 and ~10% Fe^{3+}, which further suggests that ~70% of the local pristine FeF_2 was converted to NaF, whereas only ~30% FeF_2 was still in the form of Na_3FeF_6 after the disproportionation (much less than ~90% for the *in situ* scenario). Again, the deviation of reaction extent may come from the different electrochemical environments, where a better ionic diffusion pathway may be available in real cells. So far, the similarity of heterogeneous reaction mode and the existence of disproportionation has been generically and reproducibly observed in various locations of multiple samples. We conclude that the disproportionation process is a unique path and a valid mechanism for sodiation.

Comparing to the lithiation of FeF_2 NPs, the underlying electrochemistry of sodiation is distinct, *i.e.*, heterogeneous conversion plus disproportionation (eqs 1 and 2) in sodiation *vs* one-step direct conversion (analogous to eq 1) in lithiation. Through a disproportionation process, FeF_2 can accommodate one Na^+ per formula unit, which is one-half of the theoretical specific capacity (286 mA h/g). In this aspect, the disproportionation reaction unfavorably limited the practical charge capacity.

Based on a calculated Na–Fe–F phase diagram (Figure 5g),[33] the thermodynamic equilibrium reaction pathway for sodiation (as indicated by the arrow) should be FeF_2 (→ $NaFeF_3$) → NaF, along with reduction of Fe, which requires sufficient sodium and electrochemical potential. Certainly, the real experimental conditions would deviate from such equilibrium conditions inside the sodiating particle; thus the reaction may follow the disproportionation route to form the Na_3FeF_6 phase. It is worth noting that a similar lithium ternary phase ($Li_{3/2}Fe_{1/2}F_3$) has only been theoretically predicted as an intermediate step during lithiation in the Fe^{3+} conversion system of FeF_3/Li.[34] Besides, it was also suggested in the Fe^{2+} conversion system of FeF_2/Li that a disproportionation reaction could possibly occur, in which Fe^{2+} transformed to Fe^0 and Fe^{3+} followed by simultaneous reduction of Fe^{3+} by insertion of Li.[35] That hypothesis may be useful to explain our sodiation scenario as indicated in eq 2. In addition, our experimental results suggest that the disproportionation reaction likely takes place under a Na-deficient environment. Furthermore, such a kinetics-limiting process would give rise to a critical particle size, below which the disproportionation reaction will not occur. However, due to the large deviation of diffusivity in the complicated and nontrivial electrochemical environment, it is difficult to estimate a precise value. On the other hand, phase transition from Na_3FeF_6 to NaF is possible, since *ex situ* sodiated materials have only 10% Fe^{3+}, less than 30% Fe^{3+} found in the *in situ* cell. This is consistent with a recent report on the sodiation of Na_3FeF_6 electrodes, where only a rather limited extent of Na_3FeF_6 was transformed into final products of NaF and Fe.[36] Further sodiation from Na_3FeF_6 to NaF may continue to proceed under a certain electrochemical circumstance (*e.g.*, at a lower discharging rate), but the details are still elusive. Further investigation is needed to address this question with controlling the reaction kinetics to satisfy the engineering applications. In this regard, our findings of the Na_3FeF_6 phase and disproportionation reaction may supply enlightening insights into the mechanistic understanding of the underlying electrochemistry and also stimulate more theoretical pursuits toward NIB technology.

CONCLUSIONS

In conclusion, we have carried out an in-depth investigation of the sodiation process of the FeF_2 electrode using both *in situ* and *ex situ* S/TEM techniques, which retrieved information that cannot be obtained from synchrotron XRD. Although the morphology evolution of the sodiation is identical to that of lithiation, we found that FeF_2 electrodes underwent a heterogeneous reaction mechanism with direct conversion on the surface and disproportionation reaction in the core of the particles, generating ultrafine (1–4 nm) Fe nanocrystallites and a core–shell-structured Na_3FeF_6/NaF mixture phase. In the core, the Fe nanocrystallites can be further fused into an interconnected network and coarsened under the dominance of volume diffusion. For the first time, our work revealed the disproportionation reaction in the conversion system, which provides direct evidence to confirm the prior prediction of the reaction route. The information obtained from this study is essential to understand the nanoscale sodiation in the iron fluoride system and also insightful for exploring various types of electrode materials in both LIB and NIB technologies.

METHODS

Preparation of FeF$_2$ Nanoparticles. The active material (FeF$_2$ NPs) was synthesized by a solution process from iron metal and fluorosilicic acid solutions (H_2SiF_6), as described in our prior report.[37] The as-prepared FeF$_2$ NPs were 10−20 nm in diameter and mostly in ellipsoidal shapes.

***In Situ* TEM Examination.** The *in situ* TEM experimental setup was incorporated into a Nanofactory TEM-STM specimen holder[20] (Figure 1a), in which FeF$_2$ NPs dispersed onto a TEM half-grid with amorphous carbon support are analogous to the FeFe$_2$−C composite electrode, and Na metal is coated onto a piezo-driven W probe as the counter electrode, with a thin layer of Na_2O formed on Na metal as the solid electrolyte. The Na and FeF$_2$ were loaded onto the holder in an Ar-filled glovebox and then transferred to a TEM column using a sealed Ar bag to avoid air exposure. During the *in situ* electrochemical tests, a negative potential of 3 V or higher was applied to the FeF$_2$ electrode against the Na source during the sodiation process. All the *in situ* measurements were performed on a JEOL 2100F TEM operated at 200 kV, and supplementary *ex situ* characterization was conducted on a Hitachi HD2700C scanning transmission electron microscope (STEM) operated at 200 kV and equipped with a probe aberration corrector (spatial resolution <1 Å, energy resolution 0.35 eV) and a unique secondary electron microscopy (SEM) detector.[32,38]

Battery Assembly and Testing. The composite electrodes were prepared by casting the slurry containing 66 wt % FeF$_2$, 24 wt % acetylene black, and 10 wt % polyvinylidene fluoride dissolved in *N*-methyl-2-pyrrolidone on an aluminum foil. The electrodes were dried at 60 °C under vacuum for 12 h. The electrolyte is 1 M $NaClO_4$ in ethylene carbonate/dimethyl carbonate (EC:DMC = 1:1 in volume). The CR2032-type coin cells were assembled with an FeF$_2$ electrode as the working electrode, pure Na foil as the counter electrode, and a glass fiber as the separator in an argon-filled glovebox. The galvanostatic charge/discharge was carried out on a Land BT2000 battery test system at a current density of 10 mA/g in a voltage range of 1.0−3.5 V. The cyclic voltammetry (Figure S5, Supporting Information) was measured on a Biologic battery test system. After the electrochemical tests, the coin cells were disassembled in the Ar-filled glovebox. The cycled electrode materials were collected and washed in DMC to eliminate the electrolyte residue. The active materials were then dispersed onto a Cu grid for *ex situ* TEM characterization (Figure S4, Supporting Information).

Synchrotron XRD. The samples for XRD characterization were prepared in pristine state, after the first discharge and after the first charge. The cycled materials were carefully cleaned and sealed in the glass capillary. The XRD data were collected at Beamline X14A of the National Synchrotron Light Source (NSLS) at Brookhaven National Laboratory by a linear position-sensitive silicon detector (λ = 0.7747 Å). The two-theta angles of all the XRD spectra (Figure S6, Supporting Information) have been recalculated and converted to their corresponding angles for λ = 1.54 Å, which is the wavelength of a conventional X-ray tube source with Cu Kα radiation, for easy comparison with other published results.

Conflict of Interest: The authors declare no competing financial interest.

Acknowledgment. This research was carried out at the Center for Functional Nanomaterials, Brookhaven National Laboratory, which is supported by the U.S. Department of Energy, Office of Basic Energy Sciences, under Contract No. DE-AC02-98CH10886. This work was partially supported by the Northeastern Center for Chemical Energy Storage, an Energy Frontier Research Center funded by the U.S. DOE, BES under Award No. DE-SC0001294.

Supporting Information Available: Live STEM/ED movie clips and supplementary STEM/EELS characterization of FeF$_2$ during *in situ* sodiation; TEM, ED, EELS, and XRD comparison between *in situ* and *ex situ* sodiation; and cyclic voltammetry of FeF$_2$/Na coin cells. This material is available free of charge *via* the Internet at http://pubs.acs.org.

REFERENCES AND NOTES

1. Armand, M.; Tarascon, J. M. Building Better Batteries. *Nature* **2008**, *451*, 652–657.
2. Dunn, B.; Kamath, H.; Tarascon, J. M. Electrical Energy Storage for the Grid: A Battery of Choices. *Science* **2011**, *334*, 928–935.
3. Goodenough, J. B.; Kim, Y. Challenges for Rechargeable Li Batteries. *Chem. Mater.* **2010**, *22*, 587–603.
4. Tarascon, J. M. Is Lithium the New Gold? *Nat. Chem.* **2010**, *2*, 510–510.
5. Palomares, V.; Serras, P.; Villaluenga, I.; Hueso, K. B.; Carretero-González, J.; Rojo, T. Na-Ion Batteries, Recent Advances and Present Challenges to Become Low Cost Energy Storage Systems. *Energy Environ. Sci.* **2012**, *5*, 5884–5901.
6. Slater, M. D.; Kim, D.; Lee, E.; Johnson, C. S. Sodium-Ion Batteries. *Adv. Funct. Mater.* **2013**, *23*, 947–958.
7. Pan, H.; Hu, Y. S.; Chen, L. Room-Temperature Stationary Sodium-Ion Batteries for Large-Scale Electric Energy Storage. *Energy Environ. Sci.* **2013**, *2*, 2338–2360.
8. Kim, S. W.; Seo, D. H.; Ma, X.; Ceder, G.; Kang, K. Electrode Materials for Rechargeable Sodium-Ion Batteries: Potential Alternatives to Current Lithium-Ion Batteries. *Adv. Energy Mater.* **2012**, *2*, 710–721.
9. Cabana, J.; Monconduit, L.; Larcher, D.; Palacín, M. R. Beyond Intercalation-Based Li-Ion Batteries: The State of the Art and Challenges of Electrode Materials Reacting through Conversion Reactions. *Adv. Mater.* **2010**, *22*, E170–E192.
10. Klein, F.; Jache, B.; Bhide, A.; Adelhelm, P. Conversion Reactions for Sodium-Ion Batteries. *Phys. Chem. Chem. Phys.* **2013**, *15*, 15876–15887.
11. Poizot, P.; Laruelle, S.; Grueon, S.; Dupont, L.; Tarascon, J. M. Nano-Sized Transition-Metal Oxides as Negative-Electrode Materials for Lithium-Ion Batteries. *Nature* **2000**, *407*, 496–499.
12. Kim, T. B.; Choi, J. W.; Ryu, H. S.; Cho, G. B.; Kim, K. W.; Ahn, J. H.; Cho, K. K.; Ahn, H. J. Electrochemical Properties of Sodium/Pyrite Battery at Room Temperature. *J. Power Sources* **2007**, *174*, 1275–1278.
13. Kim, J. S.; Kim, D. Y.; Cho, G. B.; Nam, T. H.; Kim, K. W.; Ryu, H. S.; Ahn, J. H.; Ahn, H. J. The Electrochemical Properties of Copper Sulfide as Cathode Material for Rechargeable Sodium Cell at Room Temperature. *J. Power Sources* **2009**, *189*, 864–868.
14. Li, X.; Hasan, M. M.; Hector, A. L.; Owen, J. R. Performance of Nanocrystalline Ni_3N as a Negative Electrode for Sodium-Ion Batteries. *J. Mater. Chem. A* **2013**, *1*, 6441–6445.
15. Nishijima, M.; Gocheva, I. D.; Okada, S.; Doi, T.; Yamaki, J.; Nishida, T. Cathode Properties of Metal Trifluorides in Li and Na Secondary Batteries. *J. Power Source* **2009**, *190*, 558–562.
16. Badway, F.; Pereira, N.; Cosandey, F.; Amatucci, G. G. Carbon-Metal Fluoride Nanocomposite: Structure and Electrochemistry of FeF_3:C. *J. Electrochem. Soc.* **2003**, *150*, A1209–A1218.
17. Li, H.; Balaya, P.; Maier, J. Li-Storage *via* Heterogeneous Reaction in Selected Binary Metal Fluorides and Oxides. *J. Electrochem. Soc.* **2004**, *151*, A1878–A1885.

18. Rangan, S.; Thorpe, R.; Bartynski, R. A.; Sina, M.; Cosandey, F.; Celik, O.; Mastrogiovanni, D. D. T. Conversion Reaction of FeF_2 Thin Films upon Exposure to Atomic Lithium. *J. Phys. Chem. C* **2012**, *116*, 10498–10503.
19. Wang, F.; Robert, R.; Chernova, N. A.; Pereira, N.; Omenya, F.; Badway, F.; Hua, X.; Ruotolo, M.; Zhang, R.; Wu, L.; *et al.* Conversion Reaction Mechanisms in Lithium Ion Batteries: Study of the Binary Metal Fluoride Electrodes. *J. Am. Chem. Soc.* **2011**, *133*, 18828–18836.
20. Wang, F.; Yu, H. C.; Chen, M. H.; Wu, L.; Pereria, N.; Thornton, K.; Van der Ven, A.; Zhu, Y.; Amatucci, G. G.; Graetz, J. Tracking Lithium Transport and Electrochemical Reactions in Nanoparticles. *Nat. Commun.* **2012**, *3*, 1201.
21. Wang, C. M.; Xu, W.; Liu, J.; Choi, D. W.; Arey, B.; Saraf, L. V.; Zhang, J. G.; Yang, Z. G.; Thevuthasan, S.; Baer, D. R.; *et al.* *In Situ* Transmission Electron Microscopy and Spectroscopy Studies of Interfaces in Li Ion Batteries: Challenges and Opportunities. *J. Mater. Res.* **2010**, *25*, 1541–1547.
22. Huang, J. Y.; Zhong, L.; Wang, C. M.; Sullivan, J. P.; Xu, W.; Zhang, L. Q.; Mao, S. X.; Hudak, N. S.; Liu, X. H.; Subramanian, A.; *et al.* *In Situ* Observation of the Electrochemical Lithiation of a Single SnO_2 Nanowire Electrode. *Science* **2010**, *330*, 1515–1520.
23. McDowell, M. T.; Ryu, I.; Lee, S. W.; Wang, C. M.; Nix, W. D.; Cui, Y. Studying the Kinetics of Crystalline Silicon Nanoparticle Lithiation with *In Situ* Transmission Electron Microscopy. *Adv. Mater.* **2012**, *24*, 6034–6041.
24. Wang, J. W.; Liu, X. H.; Mao, S. X.; Huang, J. Y. Microstructural Evolution of Tin Nanoparticles during *In Situ* Sodium Insertion and Extraction. *Nano Lett.* **2012**, *12*, 5897–5902.
25. Gu, M.; Kushima, A.; Shao, Y.; Zhang, J. G.; Liu, J.; Browning, N. D.; Li, J.; Wang, C. M. Probing the Failure Mechanism of SnO_2 Nanowires for Sodium-Ion Batteries. *Nano Lett.* **2013**, *13*, 5203–5211.
26. Su, Q.; Du, G.; Zhang, J.; Zhong, Y.; Xu, B.; Yang, Y.; Neupane, S.; Li, W. *In Situ* Transmission Electron Microscopy Observation of Electrochemical Sodiation of Individual Co_9S_8-Filled Carbon Nanotubes. *ACS Nano* **2014**, *8*, 3620–3627.
27. Huang, F.; Zhang, H.; Banfield, J. F. Two-Stage Crystal-Growth Kinetics Observed during Hydrothermal Coarsening of Nanocrystalline ZnS. *Nano Lett.* **2003**, *3*, 373–378.
28. Croft, W. J.; Kestigian, M. The Crystallography of Na_3FeF_6. *Mater. Res. Bull.* **1968**, *3*, 571–575.
29. Lin, F.; Nordlund, D.; Weng, T. C.; Zhu, Y.; Ban, C.; Richards, R.; Xin, H. L. Phase Evolution for Conversion Reaction Electrodes in Lithium-Ion Batteries. *Nat. Commun.* **2014**, *5*, 3356.
30. Garvie, L. A. J.; Buseck, P. R. Ratios of Ferrous to Ferric Iron from Nanometer-Sized Areas in Minerals. *Nature* **1998**, *396*, 667–670.
31. Cosandey, F.; Al-Sharab, J. F.; Badway, F.; Amatucci, G. G.; Stadelmann, P. EELS Spectroscopy of Iron Fluorides and FeF_x/C Nanocomposite Electrodes Used in Li-Ion Batteries. *Microsc. Microanal.* **2007**, *13*, 87–95.
32. Zhu, Y.; Inada, H.; Nakamura, K.; Wall, J. Imaging Single Atoms Using Secondary Electrons with an Aberration-Corrected Electron Microscope. *Nat. Mater.* **2009**, *8*, 808–812.
33. Jain, A.; Ong, S. P.; Hautier, G.; Chen, W.; Richards, W. D.; Dacek, S.; Cholia, S.; Gunter, D.; Skinner, D.; Ceder, G.; *et al.* The Materials Project: A Materials Genome Approach to Accelerating Materials Innovation. *APL Mater.* **2013**, *1*, 011002.
34. Doe, R. E.; Persson, K. A.; Meng, Y. S.; Ceder, G. First-Principle Investigation of the Li-Fe-F Phase Diagram and Equilibrium and Nonequilibrium Conversion Reactions of Iron Fluorides with Lithium. *Chem. Mater.* **2008**, *20*, 5274–5283.
35. Yamakawa, N.; Jiang, M.; Key, B.; Grey, C. P. Identifying the Local Structures Formed during Lithiation of the Conversion Material, Iron Fluoride, in a Li Ion Battery: A Solid-State NMR, X-ray Diffraction and Pair Distribution Function Analysis Study. *J. Am. Chem. Soc.* **2009**, *131*, 10525–10536.
36. Shakoor, R. A.; Lim, S. Y.; Kim, H.; Nam, K. W.; Kang, J. K.; Kang, K.; Choi, J. W. Mechanochemical Synthesis and Electrochemical Behavior of Na_3FeF_6 in Sodium and Lithium Batteries. *Solid State Ionics* **2012**, *218*, 35–40.
37. Pereira, N.; Badway, F.; Wartelsky, M.; Gunn, S.; Amatucci, G. G. Iron Oxyfluorides as High-Capacity Cathode Materials for Lithium Batteries. *J. Electrochem. Soc.* **2009**, *156*, A407–A416.
38. Su, D.; Wang, F.; Ma, C.; Jiang, N. Engineering Nano-Composite $Li_4Ti_5O_{12}$ Anodes *via* Scanning Electron-Probe Fabrication. *Nano Energy* **2013**, *2*, 343–350.